Three-Dimensional Radiative Wireless Power Transfer for the Internet of Batteryless Things: Modeling and Experiments

Ye Liu, *Senior Member, IEEE*, Honggang Wang *Fellow, IEEE*, and Mikael Gidlund, *Fellow, IEEE*

***Abstract*— Industrial Informatics increasingly relies on Industrial IoT sensing for predictive maintenance and digital-twin services, yet battery replacement is costly and disruptive. Radiative wireless power transfer (RWPT) can enable the Internet of Batteryless Things, but most prior analyses assume 2-D, static, line-of-sight (LOS) conditions, limiting their use for industrial deployment planning. This paper proposes a 3-D RWPT modeling and evaluation framework that couples 3-D geometry and mobility, LOS/NLOS propagation with shadowing and multipath, azimuth/elevation misalignment, and nonlinear RF-to-DC conversion with storage dynamics to predict DC energy availability. The framework outputs planner-facing KPIs, including received-power distributions, time-to-threshold charging, and service feasibility in industrial spaces. Measurements with a commercial Powercast 915-MHz kit in realistic 3-D scenarios (altitude variation, cluttered indoor environments, and through-wall NLOS) provide experimental support for the model and reveal severe attenuation (path-loss exponent up to 15.5) and order-of-magnitude power loss under orientation offsets. These results provide actionable guidance for batteryless IIoT design.**

***Index Terms*— Wireless Power Transfer, 3D deployment, Internet of Batteryless Things, Zero-energy devices, Theoretical modeling, Experimental study.**

I. Introduction

THE rapid advancement of networked embedded systems and energy-harvesting technologies has enabled the vision of the Internet of Batteryless Things (IoBT) [1], where sensing and communication devices operate without conventional batteries by harvesting energy from the environment [2]. In industrial informatics and IIoT deployments, the motivation is especially strong: battery replacement is not merely inconvenient, but operationally expensive and sometimes infeasible due to safety procedures, access constraints, high asset density, and downtime costs. In real industrial process automation deployments, practical wireless system design is often governed by maintenance constraints and service requirements rather than by link-budget metrics alone [3], [4]. Consequently, for industrial informatics, an IoBT solution is only valuable insofar as it can be translated into schedulable, planner-facing outcomes: how often a node can report, which parts of a production line can sustain that reporting interval, and how many batteryless devices can be supported under given hardware and regulatory limits.

Wireless power transfer (WPT) [5], [6] is a key enabler for batteryless operation. Non-radiative WPT techniques (e.g., inductive and resonant coupling) are effective at very short distances, whereas radiative wireless power transfer (RWPT) [7], [8] can energize distributed devices over meter-scale and beyond using RF waves, making it attractive for IoBT and IIoT deployments. A substantial literature [9] has addressed RWPT components such as rectenna design, waveform strategies, and charging scheduling. However, much of the existing modeling and analysis assume simplified operating conditions [10], [11], often two-dimensional (2D), static, and line-of-sight (LOS), which can significantly misestimate harvested energy and charging time in real industrial environments.

Industrial sites are intrinsically three-dimensional (3D) and frequently non-line-of-sight (NLOS) [12]: transmitters and receivers may be mounted at different heights; devices may rotate, tilt, or vibrate relative to antenna boresight; metallic structures, machinery, and moving assets can intermittently obstruct LOS; and strong multipath can create spatially varying power fields. These effects introduce variability that directly affects DC-level outcomes and thus the feasibility of industrial tasks: whether a sensor reaches an operational voltage in time, how much usable energy is available over a service interval, and whether a target reporting cadence can be maintained across the physical layout. For example, in rotating machinery and conveyor monitoring, engineers must guarantee that vibration/temperature sensors sustain a required reporting interval along a line or area despite 3D occlusions and device orientation changes.

Motivated by this industrial need, this paper presents a comprehensive 3D RWPT modeling framework for IoBT that

This work was supported in part by the Marie Skłodowska-Curie Actions (MSCA) Postdoctoral Fellowship MILESTONE-6G under Grant No. 101201988, and in part by the Knowledge Foundation research profile NIIT.

Ye Liu is with the Department of Graduate Computer Science and Engineering, Katz School of Science and Health, Yeshiva University, New York, NY 10016 USA and the Department of Computer and Electrical Engineering, Mid Sweden University, 85170 Sundsvall, Sweden (e-mail: ye.liu@miun.se).

Honggang Wang (corresponding author) is with the Department of Graduate Computer Science and Engineering, Katz School of Science and Health, Yeshiva University, New York, NY 10016 USA (e-mail: honggang.wang@yu.edu).

Mikael Gidlund is with the Department of Computer and Electrical Engineering, Mid Sweden University, 85170 Sundsvall, Sweden (e-mail: mikael.gidlund@miun.se).

TABLE I
SUMMARY AND COMPARISON OF STATE-OF-THE-ART WORK ON THREE-DIMENSIONAL RADIATIVE WIRELESS POWER TRANSFER.

Reference	Year	Research Focus	Consideration of 3D Environment				
			Altitude	NLOS	Multipath	Doppler Effect	Angle
Lin *et al.* [13]	2023	Optimal charging schedule	✓				
Dai *et al.* [14]	2024	Charger placement					✓
Lin *et al.* [15]	2024	Charging utility		✓			✓
Yang *et al.* [16]	2024	Precise charging		✓			✓
Yang *et al.* [17]	2025	Accurate 3D charging	✓				✓
Bhalerao *et al.* [18]	2025	3D deployment	✓				
Guo *et al.* [19]	2025	3D trajectory optimization	✓				✓
This Work	2026	Practical 3D modeling framework	✓	✓	✓	✓	✓

couples: (i) 3D geometry and kinematics, (ii) LOS/NLOS propagation with multipath effects, (iii) realistic antenna orientation and angle dependence, and (iv) nonlinear RF-to-DC conversion together with storage dynamics. The objective is not to introduce a new propagation law or rectifier theory in isolation, but to provide an end-to-end 3D-to-DC pipeline that translates deployment geometry and propagation conditions into industrially meaningful metrics such as charging time, available energy, coverage, and feasible service intervals. In other words, the framework is designed to support industrial informatics workflows in which engineers plan sensing/actuation cadence, coverage regions, and device budgets under practical constraints.

To establish practical fidelity, we conduct experimental measurements using a Powercast-based testbed to validate and calibrate the RF-to-DC and storage-level behavior of the proposed pipeline under representative 3D effects (including NLOS and orientation variability). These calibrated parameters enable the framework to be used for system-level planning studies (e.g., predicting charging time and coverage under different layouts and service intervals), thereby connecting physical-layer RWPT modeling to industrial informatics decision variables. The main contributions of this work are:

- We develop an end-to-end 3D RWPT framework that integrates 3D geometry/kinematics, LOS/NLOS propagation with multipath, antenna angle/orientation dependence, and nonlinear RF-to-DC conversion with storage dynamics, yielding DC-level performance metrics.
- We formulate planner-facing KPIs (e.g., charging time to an operational threshold, available energy over a service interval, and coverage/service feasibility) that directly map RWPT outcomes to industrial informatics requirements such as reporting cadence, coverage, and supported device budgets.
- We experimentally validate and calibrate the RF-to-DC and storage-level components of the pipeline using a Powercast-based prototype under representative 3D conditions (including NLOS and orientation effects), providing practical evidence of model fidelity for batteryless device operation.

The remainder of this paper is organized as follows: Section II reviews related work. Section III presents the proposed models, and Sectionn IV discusses their relevance to industrial informatics. Section V showcases the experimental results and numerical analysis. Finally, Section VI concludes the paper.

II. RELATED WORK

Theoretical and Experimental Studies. Bruno et al. [20] provided a comprehensive overview of the foundational principles of wireless information and power transfer. Their work includes the development of analytical models for rectenna systems and explores the trade-off between information rate and delivered energy. This foundation is further expanded in [21], where the authors elaborated on the linear energy harvesting models, non-linear saturation models, and nonlinear circuit-based models. Additionally, they demonstrated multiple RWPT systems, such as multi-antenna and intelligent reflecting surface-based RWPT prototype. A detailed classification of rectifier circuits for RWPT was presented in [22], accompanied by a performance comparison among various designs. The authors in [23] proposed a practical waveform-to-energy harvesting model that anticipates average harvested power for any given waveform. Moreover, the role of computational intelligence in modeling and optimizing RWPT systems was extensively reviewed in [24]. In addition, an in-depth examination of the evolution of RWPT technologies was conducted [25], which focuses on key components such as antennas, RF-to-DC converters, and diode modeling for low-power rectifiers. Overall, these studies provide valuable insights into RWPT from the perspectives of circuit design, signal processing, and system architecture. However, they often fail to address the intricate challenges posed by three-dimensional wireless power transfer environments.

Wireless Power Transfer in 3D Environments. Conversely, a significant portion of the literature has specifically addressed RWPT in three-dimensional settings. A model was developed in [26] to formulate location-dependent power harvesting rates in three-dimensional arrangements of multiple wireless power transmitters. Optimal wireless charger placement for directional charging were proposed in [27] and [14]. Additionally, near-optimal charging scheduling strategies were proposed in [13] for three-dimensional wireless rechargeable sensor networks operating under energy constraints. Further investigations into wireless charging with Fresnel diffraction model can be found in [15], while studies addressing the

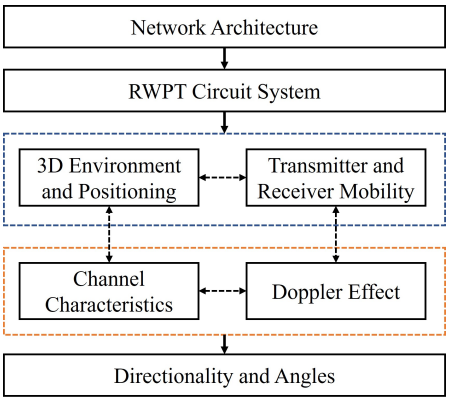

Fig. 1. End-to-end modeling chain for 3D radiative WPT.

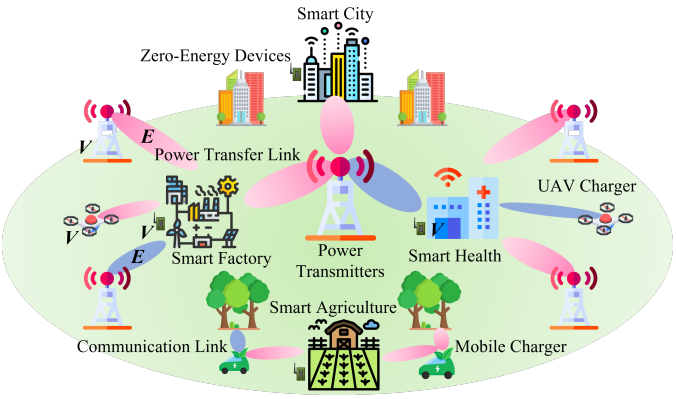

Fig. 2. Network representation of the Internet of Batteryless Things.

minimization of charging delays and precise wireless charging in complex environments have also emerged [16].

Recently, the 3D charging-utility maximization problem has been investigated in [17], where an accurate, antenna-agnostic 3D charging model and an angle–distance discretization scheme are developed to select mobile-charger positions, and the problem is cast as a submodular maximization with a performance-guaranteed approximation algorithm, achieving substantial gains over 2D-based methods in real 3D experiments. Building on aerial platforms, [18] studies the 3D deployment of autonomous aerial vehicles-mounted WPT system for IoBT by jointly optimizing the vehicle's hovering position and the harvested energy of spatially distributed sensor nodes with heterogeneous demands, formulating the problem as a Markov decision process and solving it via a soft actor–critic deep reinforcement learning algorithm with a tailored reward. In addition, [19] proposes a 3D multi-autonomous aerial vehicles framework that jointly performs far-field wireless charging and data collection for IoT devices while explicitly accounting for their average Age of Information (AoI). The NP-hard efficiency maximization problem over 3D (altitude- and velocity-aware) trajectories is addressed by a joint charging and data collection algorithm that balances data timeliness with replenishing as many devices as possible, and is validated through extensive simulations.

A summary and comparison of the state-of-the-art is presented in Table I. In contrast to the aforementioned studies that predominantly focus on the design of scheduling algorithms and operational strategies, our research aims to establish a robust modeling framework and conduct experimental studies for RWPT specifically in three-dimensional environments tailored for the Internet of Batteryless Things. By integrating fundamental principles with experimental validation, our work seeks to bridge the gap between theoretical modeling and practical application in the evolving field of IoBT.

III. 3D Environment Modeling for RWPT

To systematically capture radiative wireless power transfer in three dimensions, this section is organized as an end-to-end modeling chain, which is shown in Fig. 1. We start from the network architecture. On top of this, the RWPT circuit system specifies the actual hardware, fixing the transmit power and the RF–DC conversion behavior.

The 3D environment and positioning then place nodes in a Cartesian coordinate system and derive Euclidean distances, which are made time-varying by the transmitter and receiver mobility model so that geometry, and hence received power, become functions of time. Given these trajectories, the channel characteristics block maps transmitted to received RF power through LOS/NLOS path loss, shadowing, and multipath effects, while the Doppler effect refines this mapping in dynamic scenarios by accounting for frequency shifts due to motion.

Finally, the directionality and angles component overlays realistic 3D antenna patterns and azimuth/elevation relationships onto the channel, yielding angle-dependent gains and, ultimately, a unified model of the received RF (and corresponding DC) power field in the considered IoBT environment. This integrated structure enables the proposed model to function as a 3D RWPT framework that directly connects geometry and hardware to energy availability at batteryless devices. The remainder of this section details each of these components and shows how they are combined into a unified 3D RWPT model.

A. Network Architecture

As shown in Fig. 2, the IoBT considered in this work is characterized by a decentralized architecture consisting of many zero-energy devices and power sources distributed in a 3D volume. The network can be represented as a graph $G(V, E)$, where the vertex set V represents the nodes and the edge set E represents energy-transfer relationships.

Vertices can be categorized into two main types. Power transmitters are responsible for wirelessly transmitting energy to the batteryless nodes. These devices can be stationary or mobile, such as unmanned aerial vehicles (UAVs) and charging vehicles. Zero-energy devices receive ambient energy and may include sensors and actuators. Each device is equipped with an energy harvesting circuit to convert the received RF energy into usable electrical power. Edges in E represent energy-transfer links between nodes, signifying possible energy transfer paths. An edge exists if a receiver can harvest energy from a transmitter, which depends on distance, orientation, interference, and other environmental factors.

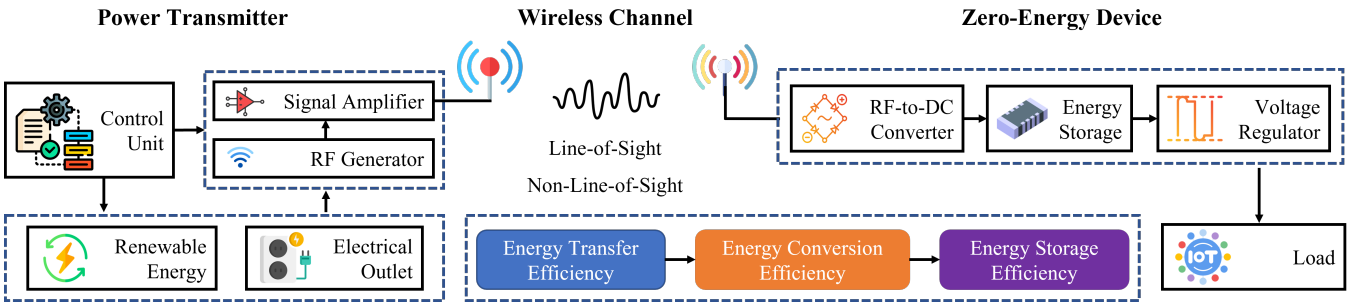

Fig. 3. Block diagram of radiative wireless power transfer circuit system in the Internet of Batteryless Things.

Node distribution refers to the spatial arrangement of power transmitters and batteryless nodes in the 3D space. The distribution can significantly impact energy transfer efficiency and overall network performance. This study examines both geometric distributions and dynamic node placement. In the former case, nodes may be uniformly or randomly distributed within a defined volume. In the latter case, node positions change over time, and locations must be represented as functions of time to capture mobility.

Moreover, routing protocols must cope with batteryless, intermittently powered devices and dynamic 3D topologies by jointly considering energy availability and spatial distribution. We highlight four representative families of approaches: (i) opportunistic routing, which forwards packets via any currently energized neighbor to exploit the time-varying energy states of zero-energy devices; (ii) energy-aware routing, which incorporates harvested/residual energy and charger proximity into its metrics to minimize end-to-end energy cost; (iii) geographic routing, which leverages 3D node positions to select next hops based on Euclidean distance; and (iv) concurrent-transmission-based routing, which uses synchronized multi-node transmissions and constructive interference to improve reliability and reduce retransmissions in ultra low-power settings.

B. RWPT Circuit System

1) Power Transmitter: As shown in Fig. 3, the RWPT circuit system consists of several critical components. The RF power transmitter is responsible for generating and emitting RF waves. It typically consists of an RF energy source, which generates a high-frequency electromagnetic signal. This energy is injected into the wireless channel through a transmitting antenna, which can be directional or omnidirectional, depending on the application and desired coverage area. To ensure efficient transmission, the system includes a signal amplifier that boosts the strength of the RF signal, allowing it to reach the receiving antenna over a greater distance. The transmitter is powered by a separate power supply, which could be connected to an electrical outlet or a renewable energy source, ensuring the continuous emission of RF energy. A control unit may be incorporated to monitor the output power, manage system efficiency, and comply with RF regulatory limits.

2) Zero-Energy Device: On the receiving end, the zero-energy device captures the radiated RF energy using a receiving antenna. The harvested energy is initially in the form of high-frequency alternating current (AC) and must be converted into direct current (DC) before it can be used. This conversion is performed by a rectifier circuit, which typically employs diodes and filtering elements to produce a DC output. Once the RF energy is converted to DC, it is either stored in an energy storage device, such as a capacitor or a rechargeable battery, or used directly to power a connected load. A voltage regulator may be employed to ensure that the output voltage remains within an acceptable range, preventing fluctuations that could cause malfunction or inefficiency. Fig. 4 illustrates the charging and discharging process captured by an oscilloscope.

3) Energy Transfer Mechanism: The energy transfer mechanism is governed by fundamental RF propagation principles. In RWPT, energy is transmitted via electromagnetic waves, typically in the radio-frequency or microwave-frequency range. The power density decreases with distance following an inverse-square law:

$$S = \frac{P_t \cdot G_t}{4\pi d^2} \tag{1}$$

where S is the power density at distance d, P_t is the transmitted power, and G_t is the gain of the transmitting antenna.

The received power can be calculated using the Friis transmission equation:

$$P_r = \frac{P_t \cdot G_t \cdot G_r \cdot \lambda^2}{(4\pi d)^2} \tag{2}$$

where P_r is the received power, G_r is the gain of the receiving antenna, and λ is the wavelength of the transmitted signal. The harvested energy over a time interval of duration t is

$$E_h = \eta_h \cdot P_r \cdot t \tag{3}$$

where η_h is the energy-conversion efficiency of the receiver.

It is worth noting that the Friis transmission equation is applicable only in the far-field region. For very small transmitter–receiver separations, the model may produce non-physical results. Similar observations have been reported in recent work, where the authors explicitly noted the near-field limitation of Friis-based modeling and adopted a modified distance term to avoid this issue [17].

4) Antenna Selection and Characteristics: The antennas utilized in RWPT are pivotal for optimizing energy transfer efficiency. The selection of the transmitting antenna influences the radiation pattern, gain, and overall transmission efficiency. The receiving antenna must also be chosen to maximize the capture of incoming RF energy. Antenna gain measures the antenna's ability to direct or concentrate RF energy. Bandwidth refers

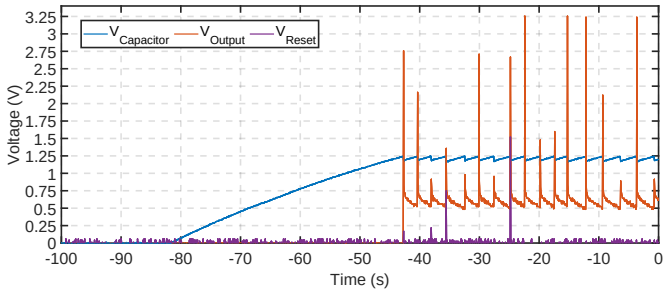

Fig. 4. Timing diagram of voltage status during wireless power transfer.

to the range of frequencies over which the antenna operates effectively. Polarization characterizes the orientation of the electromagnetic wave that the antenna is intended to transmit or receive. Common antenna types used in RWPT include patch antennas, which provide high gain and strong directivity for targeted energy transmission, and dipole antennas, which are simple, reliable, and effective over shorter distances.

C. 3D Environment and Positioning

In 3D RWPT environments, precise positioning of both the power transmitter and the receiver is essential. The positions of the power transmitter and receiver in a Cartesian coordinate system are expressed as $T(x_1, y_1, z_1)$ and $R(x_2, y_2, z_2)$, respectively. The spatial relationship between these components is described by the Euclidean distance d, which strongly impacts path loss and power-transfer efficiency:

$$d = \sqrt{(x_2 - x_1)^2 + (y_2 - y_1)^2 + (z_2 - z_1)^2}. \tag{4}$$

This expression highlights the 3D nature of the environment, with each coordinate contributing to the overall distance. Substituting (4) into (2) or the expression of NLOS in (12) produces the power received as an explicit function of positions of the 3D nodes.

D. Transmitter and Receiver Mobility

Mobility introduces additional complexity that necessitates dynamic modeling. For a UAV or ground vehicle acting as a power transmitter, the motion can be modeled as a function of time. The position of the mobile charger at time t is

$$x(t) = x_0 + v_x t, \tag{5}$$
$$y(t) = y_0 + v_y t, \tag{6}$$
$$z(t) = z_0 + v_z t, \tag{7}$$

where (x_0, y_0, z_0) are the initial coordinates and (v_x, v_y, v_z) are the velocity components. The receiver's mobility can similarly be defined, with its own velocity parameters:

$$x_r(t) = x_{r0} + v_{rx} t, \tag{8}$$
$$y_r(t) = y_{r0} + v_{ry} t, \tag{9}$$
$$z_r(t) = z_{r0} + v_{rz} t. \tag{10}$$

The distance between transmitter and receiver at time t is then

$$d(t) = \sqrt{(x_r(t) - x(t))^2 + (y_r(t) - y(t))^2 + (z_r(t) - z(t))^2}. \tag{11}$$

Through (2), (12), and (11), both P_r and the harvested power become explicit time-varying functions. In IoBT applications, mobile receivers (such as micro robotic dogs or wearable monitors) may frequently change their position, while a UAV-based transmitter can adjust its flight path dynamically to maintain effective energy delivery. This flexibility supports continuous operation of batteryless devices for real-time health monitoring and environmental sensing.

E. Channel Characteristics

Channel characteristics have a profound effect on power-transfer efficiency. We consider both line-of-sight (LOS) and non-line-of-sight (NLOS) scenarios.

1) Line-of-Sight (LOS) Conditions: In ideal LOS conditions, the transmitted power experiences minimal degradation beyond free-space path loss. The received power P_r can be approximated by the Friis equation (2), which relates P_r to the transmitted power, antenna gains, distance, and wavelength.

2) Non-Line-of-Sight (NLOS) Conditions: In many IoBT deployments, NLOS conditions are common, for example in urban settings with buildings or indoor environments with walls and furniture. NLOS propagation typically involves increased path loss and multipath effects.

a) Log-Distance Path-Loss Model: A common approach to NLOS propagation is the log-distance path-loss model (or ITU urban path-loss model), which introduces a path-loss exponent α to capture environment-dependent attenuation. The received power in NLOS can be modeled as

$$P_r = P_t G_t G_r \left(\frac{\lambda}{4\pi d_0}\right)^2 \left(\frac{d_0}{d}\right)^{\alpha} \tag{12}$$

where P_t is the transmitted power, G_t and G_r are the antenna gains, λ is the wavelength, d_0 is a reference distance (typically 1 m), d is the distance between transmitter and receiver, and α is the path-loss exponent. Typical values are $\alpha = 2$ in free space, $\alpha = 3 \sim 4$ in indoor environments, and $\alpha = 3.5 \sim 5$ in urban environments [28].

b) Shadowing and Fading Models: In real-world environments, obstacles introduce shadowing (slow fading) and multipath fading (fast fading) due to reflections, diffraction, and scattering. Shadowing can be modeled as a log-normal random variable. The received power including shadowing is

$$P_r = P_t G_t G_r \left(\frac{\lambda}{4\pi d_0}\right)^2 \left(\frac{d_0}{d}\right)^{\alpha} 10^{\chi_\sigma/10} \tag{13}$$

where χ_σ is a zero-mean Gaussian random variable with standard deviation σ (in dB).

c) Ray-Tracing Model for Multipath Propagation: Multipath propagation contributes to the received power in NLOS scenarios. As a simplified framework-level approximation, we model the total received power by summing the contributions from dominant propagation paths. For each ray i, the received power contribution is

$$P_r(i) = P_t G_t G_r \left(\frac{\lambda}{4\pi d_i}\right)^2 \Xi_i \tag{14}$$

where d_i is the path length of the i-th ray and Ξ_i is a path-dependent attenuation coefficient. In the present model, Ξ_i is

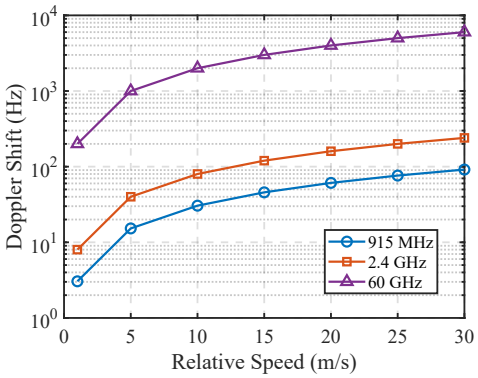

Fig. 5. Doppler shift versus relative speed for three carrier frequencies (915 MHz, 2.4 GHz, and 60 GHz).

mainly used to capture reflection-induced attenuation along the path and can be written as $\Xi_i = \prod_{k=1}^{N_i} \Gamma_k$ when reflection is dominant, where Γ_k is the reflection coefficient of the k-th surface along that path. The total received power is then

$$P_r = \sum_{i=1}^{N} P_r(i). \tag{15}$$

Accordingly, the above expression should be interpreted as a simplified multipath approximation. More detailed treatment of diffraction, obstacle geometry, surface extent, and Fresnel-zone effects can be incorporated in future extensions of the framework [16], [29].

F. Doppler Effect

When wireless power transmitters and zero-energy devices are moving, the Doppler effect induces a frequency shift in the received signal. The Doppler shift Δf_d is

$$\Delta f_d = \frac{v}{c} f_c = \frac{v}{\lambda}, \tag{16}$$

where v is the relative velocity in the direction of motion, f_c is the carrier frequency, $\lambda = c/f_c$ is the wavelength, and c is the speed of light.

For typical low / medium / high relative speeds $v \in \{1, 10, 30\}$ m/s (slow-moving conveyors or robot arms, aisle-level automated guided vehicles (AGVs) or overhead cranes, and fast UAV or rail-mounted inspection passes), the corresponding Doppler shifts are on the order of

$$\Delta f_d \approx \begin{cases} \{3,\ 30,\ 91\}\ \text{Hz} & \text{at 915 MHz}, \\ \{8,\ 80,\ 240\}\ \text{Hz} & \text{at 2.4 GHz}, \\ \{200,\ 2000,\ 6000\}\ \text{Hz} & \text{at 60 GHz}, \end{cases} \tag{17}$$

as illustrated in Fig. 5. Consequently, for the 915 MHz experimental platform and the modest UAV/AGV velocities (on the order of a few m/s), the Doppler-induced shift is at most a few tens of hertz and does not produce a measurable change in the time-averaged harvested DC power. However, at mmWave frequencies (e.g., 60 GHz) and higher UAV speeds, the Doppler effect can easily reach several kilohertz, becoming comparable to or larger than typical hardware-induced offsets. In such regimes, Doppler directly shapes the short-term power fluctuations and must be explicitly accounted for when designing rectifier bandwidths, adaptive beamforming, and charging schedules. A dedicated high-speed, mmWave WPT prototype to experimentally validate these high-Doppler regimes is therefore an important direction for future work.

G. Directionality and Angles

In 3D RWPT, the angular relationship between power transmitter and receiver has a strong impact on power-transfer efficiency due to directional antenna patterns, beamforming, and alignment. To accurately model these effects, it is necessary to account for antenna orientation, transmission angle, and angle of incidence at the receiver.

1) Antenna Orientation: Transmitter and receiver antennas are often directional, which means that radiated power varies with spatial direction. This directional property is characterized by the antenna gain pattern. The gain of the transmitting antenna depends on its orientation in spherical coordinates, specified by the azimuth angle ϕ_t and elevation angle θ_t, and can therefore be written as $G_t(\theta_t, \phi_t)$. For analytical tractability, we adopt a separable parametric approximation:

$$G_t(\theta_t, \phi_t) = G_{t,\max} \cos^{n_{\theta,t}}\left(\frac{\theta_t}{\Delta\theta_t}\right) \cos^{n_{\phi,t}}\left(\frac{\phi_t}{\Delta\phi_t}\right) \tag{18}$$

where $G_{t,\max}$ is the maximum transmit antenna gain, $\Delta\theta_t$ and $\Delta\phi_t$ denote the effective elevation and azimuth beamwidths, respectively, and $n_{\theta,t}$ and $n_{\phi,t}$ control the directional sharpness in the two angular dimensions. Here, θ_t and ϕ_t represent the elevation and azimuth misalignment angles between the transmitter boresight and the receiver direction. It is used as a tractable approximation of a 3D directional antenna pattern.

Similarly, the receiver gain $G_r(\theta_r, \phi_r)$ depends on its orientation in both elevation and azimuth. It is modeled as

$$G_r(\theta_r, \phi_r) = G_{r,\max} \cos^{n_{\theta,r}}\left(\frac{\theta_r}{\Delta\theta_r}\right) \cos^{n_{\phi,r}}\left(\frac{\phi_r}{\Delta\phi_r}\right) \tag{19}$$

where $G_{r,\max}$ is the maximum receive antenna gain, $\Delta\theta_r$ and $\Delta\phi_r$ are the effective receiver beamwidths, and $n_{\theta,r}$ and $n_{\phi,r}$ determine the directional sharpness of the receive pattern. Here, θ_r and ϕ_r denote the elevation and azimuth misalignment angles between the receiver boresight and the incoming signal direction.

The above expressions are intended as simplified parametric models for analysis and numerical evaluation. More general measured or manufacturer-provided antenna patterns can also be incorporated when available. This treatment is consistent with prior work on precise wireless charging in complicated environments, where antenna directivity is modeled in a general angle-dependent form and then adapted according to the deployment geometry [16]. In addition, the practical impact of azimuthal orientation is further examined in the experimental and numerical analysis in Section V.

2) Angle Between Transmitter and Receiver: For a given transmitter at position (x_1, y_1, z_1) and receiver at (x_2, y_2, z_2), the relative angles between them are obtained from their coordinate difference. The azimuth angle ϕ (horizontal) is

$$\phi = \tan^{-1}\left(\frac{y_2 - y_1}{x_2 - x_1}\right), \tag{20}$$

and the elevation angle θ (vertical) is

$$\theta = \tan^{-1}\left(\frac{z_2 - z_1}{\sqrt{(x_2 - x_1)^2 + (y_2 - y_1)^2}}\right). \tag{21}$$

These angles define the direction of the line-of-sight vector relative to the antenna boresights and are used in the gain models (18) and (19).

3) Power-Transfer Model with Angles: The received power accounting for directionality can be expressed as an angle-dependent extension of the Friis equation:

$$P_r = P_t\, G_t(\theta_t, \phi_t)\, G_r(\theta_r, \phi_r) \left(\frac{\lambda}{4\pi d}\right)^2 \tag{22}$$

where $G_t(\theta_t, \phi_t)$ is the transmit antenna gain in the direction of the receiver and $G_r(\theta_r, \phi_r)$ is the receive antenna gain in the direction of the transmitter. Accurate orientation and beam-steering are critical to maximizing power-transfer efficiency.

4) NLOS and Multipath Scenarios with Angles: In NLOS environments, the signal may reach the receiver through reflections, scattering, or diffraction. The angles of incidence and reflection become important: the angle of incidence equals the angle of reflection, while the effective gains along each path depend on both antenna patterns and surface properties. The total received power in such scenarios can be modeled as

$$P_r = \sum_{i=1}^{n} P_{r_i}\, G_t(\theta_{t_i}, \phi_{t_i})\, G_r(\theta_{r_i}, \phi_{r_i}) \tag{23}$$

where P_{r_i} is the power contribution from the i-th path and $G_t(\theta_{t_i}, \phi_{t_i})$, $G_r(\theta_{r_i}, \phi_{r_i})$ are corresponding directional gains.

When transmitters are moving, angles $\theta_t, \phi_t, \theta_r, \phi_r$ change over time. Real-time tracking and alignment techniques, such as adaptive beamforming and directional control, can help maintain optimal power transfer. In many-to-one or many-to-many scenarios, coordinated beamforming among multiple transmitters can be used to focus energy on specific targets while mitigating interference.

H. Mathematical Coupling of Submodels and Usage

At a high level, the proposed 3D RWPT framework is not merely a collection of individual propagation, antenna, and circuit models. Rather, it is a mathematically coupled end-to-end pipeline that maps 3D deployment and motion variables to DC-level performance metrics and planner-facing KPIs. The novelty of the framework therefore lies in the explicit integration of the above submodels into a single 3D-to-DC mapping for IoBT analysis and planning.

To make this coupling explicit, let the overall system state at time t be denoted by

$$\mathbf{s}(t) = \begin{pmatrix} x_T(t),\ y_T(t),\ z_T(t),\ x_R(t),\ y_R(t), \\ z_R(t),\ \theta_t(t),\ \phi_t(t),\ \theta_r(t),\ \phi_r(t), \mathcal{E}(t) \end{pmatrix} \tag{24}$$

where (x_T, y_T, z_T) and (x_R, y_R, z_R) are the transmitter and receiver coordinates, (θ_t, ϕ_t) and (θ_r, ϕ_r) describe antenna orientations, and $\mathcal{E}(t)$ denotes the environment state, including LOS/NLOS condition, obstacles, and multipath characteristics.

Based on this state, the overall framework can be interpreted as the following chained mapping:

$$\begin{aligned} \mathbf{s}(t) \ &\rightarrow\ P_{\mathrm{RF}}(t) \ \rightarrow\ P_{\mathrm{DC}}(t) \\ &\rightarrow\ V(t) \ \rightarrow\ \{T_{\mathrm{th}}, E_{\mathrm{avail}}, \tau, C(\tau), B(\tau)\} \end{aligned} \tag{25}$$

This compact expression clarifies how geometry, mobility, propagation, antenna directionality, and circuit behavior are coupled into a unified RWPT model.

Usage: Given a 3D trajectory of a power transmitter or receiver, $(x(t), y(t), z(t))$, the corresponding antenna orientation (θ, ϕ), and the wall/obstacle state of the environment, the framework operates as follows.

1) Geometry, Channel, and RF Power Coupling: The geometry and environment determine the Euclidean distance $d(t)$, the LOS/NLOS state, and the applicable propagation model, such as free-space propagation, log-distance path loss with exponent α, shadowing, or ray-tracing refinement. At the same time, the relative azimuth and elevation angles determine the directional antenna gains. Therefore, the received RF power is not obtained from a single isolated equation, but from the composition of the position model, mobility model, channel model, Doppler model when needed, and directional antenna model. This yields the time-varying received RF power

$$P_{\mathrm{RF}}(t) = P_r\big(\mathbf{s}(t)\big), \tag{26}$$

where $P_r(\mathbf{s}(t))$ denotes the coupled RF-domain mapping. In other words, all upstream submodels are explicitly aggregated into a single RF-power output.

2) RF-to-DC Conversion Coupling: The received RF power is then mapped to harvested DC power through the nonlinear rectification model. Let $\eta(P)$ denote the RF-to-DC conversion efficiency. The harvested DC power is

$$P_{\mathrm{DC}}(t) = \eta(P_{\mathrm{RF}}(t))\, P_{\mathrm{RF}}(t). \tag{27}$$

Equation (27) explicitly couples the RF-domain model to the circuit-domain model. Hence, any change in 3D position, motion, blockage, or antenna misalignment propagates to the DC domain through $P_{\mathrm{RF}}(t)$.

3) Storage-Dynamics Coupling: The harvested DC power then drives the energy storage element. Let $V(t)$ denote the storage voltage, C the capacitance, R_L the effective load resistance, and $\epsilon > 0$ a small regularization constant that avoids division by zero at low voltage. The voltage dynamics are modeled as

$$\dot{V}(t) = \frac{1}{C}\left(\frac{P_{\mathrm{DC}}(t)}{V(t) + \epsilon} - \frac{V(t)}{R_L}\right). \tag{28}$$

Solving Eq. (28) for a given $P_{\mathrm{DC}}(t)$ yields the voltage trajectory $V(t)$. This step couples the harvested power to the temporal evolution of usable stored energy, thereby linking physical-layer WPT behavior to device operability.

4) DC Metrics and Planner-Facing KPIs: From $V(t)$, we extract DC-level metrics such as the charging time to an operational threshold voltage V_{th},

$$T_{\mathrm{th}} = \inf\{t \geq 0 \mid V(t) \geq V_{\mathrm{th}}\}, \tag{29}$$

and the available energy in the storage element,

$$E_{\mathrm{avail}}(t) = \frac{1}{2} C \left(V^2(t) - V_{\min}^2\right), \tag{30}$$

where $V_{\min}$ is the minimum usable voltage. These quantities then determine planner-facing KPIs such as the feasible service interval τ, the coverage or task-success probability $C(\tau)$, and the number of batteryless devices that can be reliably supported $B(\tau)$. Therefore, this end-to-end formulation makes the integration of the submodels visible and provides a direct analytical path from deployment variables to practical design outcomes in IoBT applications.

IV. Relevance to Industrial Informatics and IIoT Workloads

Industrial deployments are intrinsically three-dimensional and often non-line-of-sight [12]: transmitters and receivers sit at different heights; assets rotate or tilt relative to antenna boresight; aisles, doors, and machinery intermittently occlude line-of-sight. Importantly, plant engineers and maintenance teams do not plan in terms of raw RF margins, but in terms of cadence (how often a node can report) and coverage (which parts of a line or area meet that cadence) under given hardware and cost constraints. In this context, a radiative WPT model is only useful insofar as it yields schedulable DC outcomes and directly informs industrial data and network planning. To make this link explicit, we anchor our framework in a representative IIoT workload: rotating machinery such as conveyors, rollers, and shafts, where vibration, temperature, and acoustic sensors feed maintenance analytics and alarm processing [30].

Within this workload, we interpret the 3D RWPT results entirely through planner-facing KPIs. First, we define the update interval τ that a given sensor node can sustainably support under its harvested energy budget. Second, along a conveyor or machine line, we quantify line-wise coverage at a target interval τ via

$$C(\tau) = \frac{\text{length}\{x \in \text{line} : T_{\text{th}}(x) \le \tau\}}{\text{length(line)}}, \tag{31}$$

where $T_{\text{th}}(x)$ is the charging time at position x to reach a usable voltage threshold. Third, we define a *packet budget*

$$B(\tau) = \lfloor E_{\text{avail}}(\tau)/E_p \rfloor, \tag{32}$$

which binds the available energy $E_{\text{avail}}(\tau)$ over interval τ to the energy per packet E_p (sensing plus MAC/PHY overhead), and thus to the number of data or alarm packets that can be reliably scheduled. In other words, all lower-layer results are read as constraints on sampling rate, alarm latency, and node count that the industrial network can support.

For a typical configuration with a ceiling-mounted transmitter at height h_T and a line of rotating or translating sensors at height h_R, the 3D separation (d, θ, ϕ) feeds the channel block of our framework: a LOS/NLOS log-distance model with shadowing, combined with measured antenna patterns and, where residuals indicate elevation-induced lobing, a bounded elevation-aware two-ray refinement. This yields the received RF power field $P_{\text{RF}}(x)$ along the line. The RF field is then mapped to DC via the device-specific, monotone RF-to-DC conversion curve $\eta(P)$, $P_{\text{DC}}(x)$, and injected into the storage dynamics of the energy buffer. It yields the voltage trajectory $V(t)$, the threshold crossing time $T_{\text{th}} = \inf\{t : V(t) \ge V_{\text{th}}\}$,

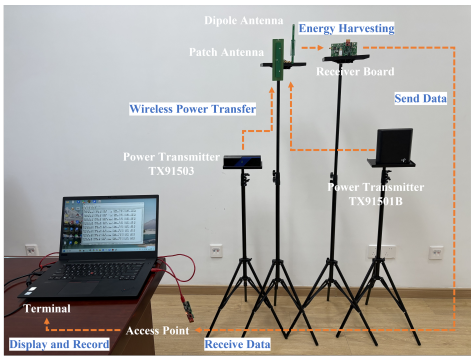

Fig. 6. Experimental study utilizing the state-of-the-art Powercast Development Kit.

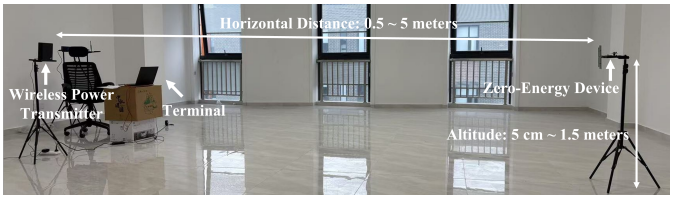

Fig. 7. Experimental analysis in LOS scenario across varying horizontal distances and altitudes.

and the available energy $E_{\text{avail}}(t) = \frac{1}{2}C\left(V^2(t) - V_{\min}^2\right)$. At 915 MHz, carrier Doppler for typical belt speeds $v \in [0.5, 1]$ m/s is small (on the order of 1.5–3.1 Hz), but indoor multipath still induces envelope variability. Therefore, it is necessary to report 1 dB level-crossing rates and fade depths along 3–5 m traces (sampled at ≥ 50 Hz) and propagate this variability into uncertainty bands on T_{th} and $C(\tau)$, so that planners can reason about robustness, not only averages.

This example illustrates how the proposed 3D RWPT framework directly supports industrial informatics by turning detailed RF and energy models into concrete, schedulable design rules for IIoT sensing and communication networks.

V. Experimental Study

This section presents an experimental study of radiative WPT in a three-dimensional environment, highlighting the significant impact of various settings on received power. In the experimental platform shown in Fig. 6, the receiver is implemented as a batteryless sensing node based on the Powercast P2110-EVB and WSN-EVAL-01 platform. The P2110-EVB harvests RF energy through the receiving antenna and supplies power to the attached WSN-EVAL-01 sensor board. After sufficient energy has been accumulated, the sensor board performs sensing tasks, such as temperature, humidity, and ambient-light measurement, and then wirelessly transmits the sensed data to an access point (AP). The packet arrivals recorded at the AP therefore reflect the completion of a sensing-and-transmission cycle supported by the harvested RF energy. In addition, each transmitted packet reports a vendor-defined received-power/RSSI indication associated with the harvesting system, which is used in this work as an observable indicator of the power-transfer condition. Key parameters of these components are summarized in Table II. Additionally,

TABLE II
KEY PARAMETERS OF THE LEADING COMMERCIAL WIRELESS POWER TRANSFER PRODUCTS DEVELOPED BY POWERCAST.

Component	Model	Frequency Range	Power (Output or Input)	Gain	Radiation Pattern	Polarization	Return Loss
Power Transmitter	TX91501B	915 MHz (Center)	3W EIRP	8 dBi	H: 60° V: 60°	Vertical	-
Power Transmitter	TX91503	915 MHz (Center)	3W EIRP	6 dBi	H: 70° V: 130°	Horizontal	-
Receiving Antenna	PA-915-01	902 - 928 MHz	-	6.8 dBi	H: 122° V: 68°	Vertical	< -10 dB
Receiving Antenna	DA-915-01	902 - 928 MHz	-	1.7 dBi	Omni-directional	Vertical	< -10 dB
Receiver Board	P2110-EVB	902 - 928 MHz	-12-10 dBm	-	-	-	–

Abbreviations: Watts (W); Effective Isotropic Radiated Power (EIRP); Horizontal (H); Vertical (V).

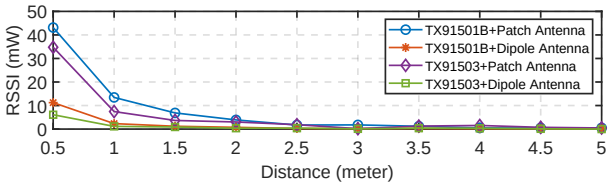

(a) Experimental results

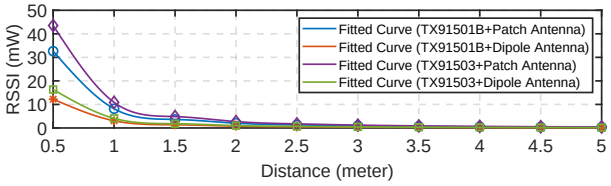

(b) Numerical results

Fig. 8. Results of received signal strength indicator in LOS scenario with different horizontal distances.

numerical analysis using MATLAB was conducted to validate the effectiveness of the proposed models, which align closely with the experimental results.

A. Impact of Distance and Altitude

We first present the basic results regarding the impact of horizontal distance on received power. The experimental setup is illustrated in Fig. 7. The altitude of both the wireless power transmitter and the zero-energy device is fixed at 1 meter. The horizontal distance is gradually increased from 0.5 to 5 meters in increments of 0.5 meters. The experimental results in Fig. 8a indicate a clear trend. As the horizontal distance increases, the received power decreases, demonstrating the inverse relationship described by the Friis transmission equation. Specifically, at a distance of 0.5 meters, the received power is at its maximum, while at 5 meters, the power significantly diminishes. The numerical results in Fig. 8b were calculated using Equation 2 and the Powercast Wireless Power Calculator. These results align closely with the experimental findings, confirming the predictions made by the Friis transmission equation.

As altitude is a key factor in a three-dimensional environment, we conducted an experimental study to investigate its impact on received power. In this study, we fixed the horizontal distance between the power transmitter and the zero-energy device at 50 centimeters and 1 meter, while varying the altitude synchronously at three levels: 5 cm, 50 cm, and 150 cm. As illustrated in Fig. 9a and Fig. 9b, the results reveal significant fluctuations in received power across all four deployment settings. A primary reason for this variability is multipath propagation due to ground reflection. At lower altitudes (5 cm and 50 cm), the proximity to the ground results in stronger reflections that can lead to either constructive or destructive interference with the direct signal, causing variations in received power. However, as the altitude increases to 150 cm, the effect of ground reflection diminishes, allowing the direct signal to dominate the received power. Overall, these findings underscore the importance of considering altitude and its effects on multipath propagation in the design of effective radiative wireless power transfer systems within three-dimensional environments.

It is worth noting that this experiment intentionally focuses on a short-range (< 5m) configuration. This choice is motivated by three considerations. First, these short-range links are representative of many industrial informatics and IIoT deployments, where WPT transmitters are mounted on ceilings, walls, or machinery frames, and power vibration/temperature/acoustic sensors on conveyors, rollers, shafts, tanks, or cabinets typically within a few meters. Therefore, such a charging distance is a realistic first-order approximation of the operating conditions that plant engineers actually design for. Second, the controlled short-range baseline, together with the Friis-based model, also reveals concrete levers for extending the effective charging distance in practice: increasing link budget via higher-gain or beam-steered antennas, deploying multiple coordinated transmitters along production lines, and reducing the power demand of zero-energy devices through more efficient rectifiers and ultra-low-power sensing/communication stacks. All these techniques effectively increase the margin between received power and sensitivity, enabling the same minimum harvested power to be sustained at larger distances in future IIoT deployments. Third, due to space constraints in indoor venues, the maximum test distance considered in this work is 5 m. In our previous work, we conducted field measurements in outdoor scenarios. With the current commercial 915 MHz WPT testbed, the maximum achievable measurement distance can reach up to 12 m. Moreover, the multipath effect formed indoors can provide constructive combining and further extend the effective charging range to over 40 m, while the majority of data transmission intervals are typically on the order of tens of seconds [11].

On the other hand, although the reported received power levels are in the mW range (typically from a few milliwatts up to about 50 mW), this is in fact compatible with the

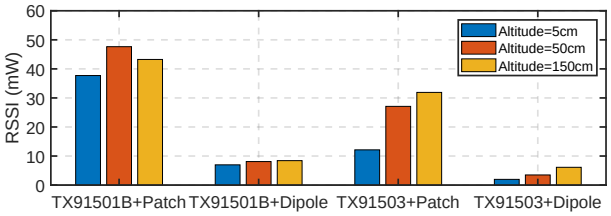

(a) Horizontal distance = 50 centimeters

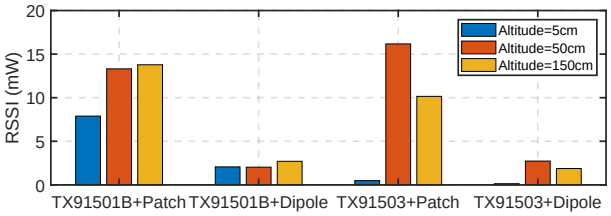

(b) Horizontal distance = 1 meter

Fig. 9. Results of received signal strength indicator in LOS scenario with different altitudes.

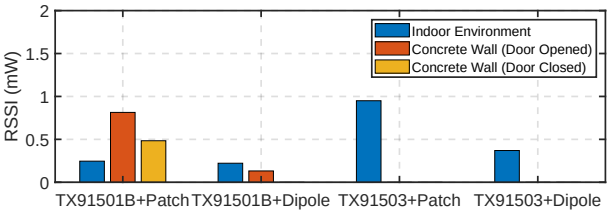

(a) Experimental results of RSSI

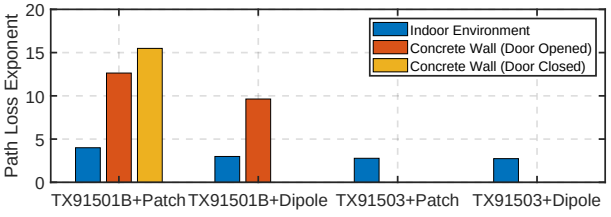

(b) Numerical results of path loss exponent

Fig. 11. Results of received signal strength indicator and path loss exponent in NLOS scenarios.

(a) Indoor environment (b) Concrete wall

Fig. 10. Experimental setup in NLOS scenarios.

ultra-low-power sensing workloads targeted in IoBT applications. For typical batteryless sensor nodes, a single sensing–processing–transmission cycle consumes on the order of 10^1–10^2 μJ, so an average harvested DC power of 1 mW can replenish the energy for one such cycle in roughly 0.1 s, and even lower average power (tens to hundreds of μW) is sufficient for reporting intervals in the range of seconds to minutes. In other words, the measured few–50 mW RF levels, when interpreted through the RF–DC conversion and storage models, are adequate to sustain duty-cycled vibration/temperature/acoustic monitoring and low-rate data transmission in industrial informatics scenarios, especially when combined with energy-aware scheduling.

B. Impact of Non-Line-of-Sight Conditions

In the following, we investigate radiative wireless power transfer under non-line-of-sight conditions, specifically within an office environment to assess received power levels. Fig. 10a illustrates the indoor office setup, where various materials, including desks, computers, and bookshelves, are positioned along the wireless power transfer path. The distance between the wireless power transmitter and the zero-energy device is 2.4 meters. Conversely, Fig. 10b depicts a scenario in which the wireless power transmitter is located inside the office while the zero-energy device is placed outside, separated by a 20-centimeter thick concrete wall. In this setup, both the power transmitter and the zero-energy device are positioned 50 centimeters away from the wall.

Fig. 11a presents the experimental results. The TX91501B power transmitter, paired with a patch antenna on the receiver, performs adequately in all tested scenarios (indoor environment, concrete wall with both doors opened and closed). However, the wireless power transfer demonstrates significant degradation when other component configurations are employed, particularly when the door is closed. This reduced performance can be attributed to increased signal attenuation caused by the obstruction of the wall and closed door, as well as additional multipath effects and interference from surrounding materials that can scatter or absorb the transmitted power. Additionally, we calculated the path loss exponent using Equation 12. As shown in Fig. 11b, the values obtained for the four configurations (TX91501B with patch receiving antenna, TX91501B with dipole receiving antenna, TX91503 with patch receiving antenna, and TX91503 with dipole receiving antenna) were found to be 3.99, 2.99, 2.78, and 2.74, respectively. These results align closely with empirical values observed in indoor environments, further validating the effectiveness of the established model. Notably, the path loss exponent escalates to as high as 15.48 when faced with substantial obstacles such as a thick concrete wall, indicating a significant degradation in power transfer efficiency. The insights derived from these findings underscore the challenges of wireless power transfer in three-dimensional environments, particularly when obstructions are present. The results suggest that optimizing transmitter and receiver placements, as well as considering the effects of environmental materials, are crucial for enhancing power transfer efficiency.

It is worth mentioning that these NLOS experiments are not intended to exhaustively capture all possible “realistic 3D environments”, but rather to calibrate and validate the NLOS component of the proposed 3D RWPT framework under two representative conditions: (i) cluttered indoor propagation with furniture and equipment along the path, and (ii) severe

(a) Azimuth angles (b) Elevation angles

Fig. 12. Experimental setup for varying orientations.

through-wall attenuation across a structural concrete barrier. In a full 3D deployment, additional factors such as multi-wall propagation, floor-to-floor coupling, and more complex 3D geometries will further shape the harvested-power field. However, the measured path loss exponents and through-wall attenuation reported here provide concrete parameter ranges and worst-case bounds for the NLOS and shadowing models in Section III, which are then used to construct 3D harvested-power maps in more general layouts.

In particular, by combining these empirically derived parameters with the log-distance and ray-based models, scenario-specific 2D/3D performance heatmaps (e.g., received power, harvested power, or charging time) can be generated for actual rooms, corridors, or industrial cells, providing a practical tool for planning transmitter/receiver placement. Extending the experimental campaign to a wider variety of 3D NLOS scenarios (e.g., multi-floor industrial halls, dense shelving, and metallic structures) is important, but even this focused study already quantifies how realistic indoor clutter and structural walls can dramatically impact radiative WPT, and thus must be explicitly accounted for in 3D planning and placement.

C. Impact of Angles

Finally, we investigate the impact of orientation on the received power. Fig. 12a and 12b illustrate the experimental setup. In the first scenario, the radius from the power transmitter to the zero-energy device is set to 1 meter. The azimuth angle is varied horizontally from 0° to 180° in increments of 30°. Fig. 13a presents the experimental results for received power across the different azimuth angles. Notably, the highest power transfer occurs at a face-to-face alignment of 90°, where received power reaches its peak. As the azimuth angle deviates from 90°, there is a sharp decline in the received power values, indicating that optimal alignment is crucial for effective wireless power transfer.

In existing simplified 2D models, the power transmitter and receiver are implicitly assumed to be perfectly aligned in the horizontal plane, which corresponds exactly to the 90° face-to-face case in our evaluation. Under this assumption, the received power is treated as a function of distance only, and the strong dependence on azimuth is completely neglected. Our measurements, however, show that deviations from 90° can reduce the harvested power by orders of magnitude compared to the face-to-face case, even at the same radius. This highlights that azimuthal orientation is a first-order design

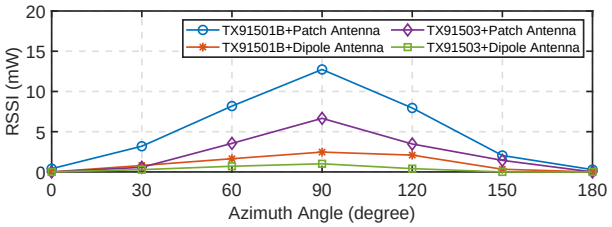

(a) Experimental results across varying azimuth angles

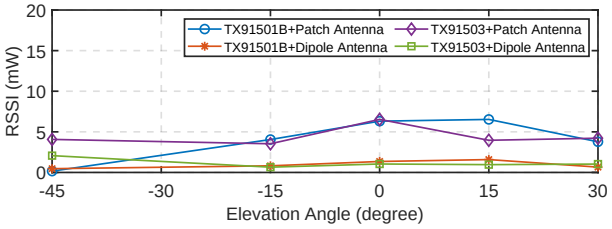

(b) Experimental results across varying elevation angles

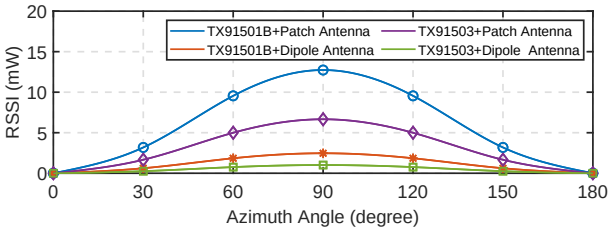

(c) Numerical results across varying azimuth angles

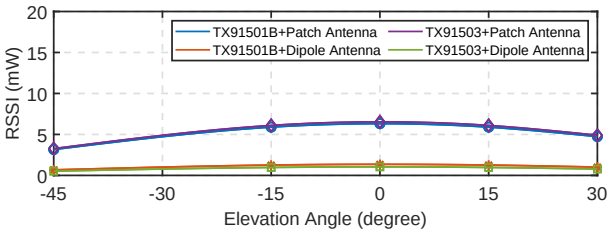

(d) Numerical results across varying elevation angles

Fig. 13. Results of received signal strength indicator with varying orientations.

factor for practical RWPT deployments, and that simplistic 2D models are prone to systematically overestimating the harvested power for misaligned IoBT devices.

In the second scenario, the radius from the power transmitter to the zero-energy device is adjusted to 1.414 meters, and the elevation angle is varied from -45° to 30°. The experimental results of received power across the varying elevation angles are shown in Fig. 13b. The received power values exhibit fluctuations, which can be attributed to factors such as ground reflection and the antenna radiation pattern. These variations highlight the complexities introduced by changes in elevation, emphasizing the significance of environmental conditions on power transfer efficiency.

Similarly, in simplified 2D models the transmitter and receiver are typically assumed to lie in the same horizontal

plane, which corresponds to the 0° elevation case in our evaluation. Under this assumption, the vertical geometry and ground-reflection effects are effectively collapsed, and the received power is again treated as a pure function of distance. Our measurements, however, show fluctuations and local minima/maxima as the elevation angle varies from -45° to 30°. This implies that a 2D model centered on the 0° elevation case can misestimate the harvested power for devices mounted above or below the nominal plane, leading to overly optimistic coverage predictions and misdimensioned energy budgets in realistic 3D deployments.

To further validate our findings, we compute numerical results using the theoretical model derived from Eq. (22). As depicted in Fig. 13c and 13d, the numerical results for different azimuth angles closely align with the experimental data, confirming the effectiveness of our models. However, the numerical and experimental results for varying elevation angles do not match perfectly. This discrepancy primarily arises because the numerical calculations do not account for multipath effects, which are significant in real-world scenarios. For a more accurate representation, it is necessary to employ Eq. (23), which incorporates complex factors such as multipath and NLOS conditions. By including these elements, we can achieve a more comprehensive understanding of the wireless power transfer dynamics in various orientations.

VI. Conclusion

This study set out to develop models and conduct experimental investigations for IoBT in 3D environments. We first developed a theoretical framework to model RWPT, accounting for network architecture, circuit system, 3D environmental factors, positioning, mobility of power transmitters and receivers, channel characteristics, the Doppler effect, and directionality. We then conducted experimental studies to assess the impact of these factors on the received power at zero-energy devices. The findings highlight the critical role of considering altitude, NLOS conditions, and node orientations in optimizing power transfer efficiency. The numerical analysis further corroborated our findings, demonstrating a strong alignment between the experimental and theoretical results, which validates the effectiveness of the proposed models.

References

[1] S. Ahmed *et al.*, "The Internet of Batteryless Things," *Communications of the ACM*, vol. 67, no. 3, p. 64–73, feb 2024.

[2] Y. Liu *et al.*, "Understanding the Impact of Environmental Conditions on Zero-Power Internet of Things: An Experimental Evaluation," *IEEE Wireless Communications*, vol. 30, no. 6, pp. 152–159, 2023.

[3] A. Ahlen *et al.*, "Toward Wireless Control in Industrial Process Automation: A Case Study at a Paper Mill," *IEEE Control Systems Magazine*, vol. 39, no. 5, pp. 36–57, 2019.

[4] Z. Xu *et al.*, "Intermittently Dynamic Fuzzy Learning-Based Tracking Control of Amplitude Signals for Vibratory Gyroscopes With Composite Identification," *IEEE Transactions on Instrumentation and Measurement*, vol. 74, pp. 1–8, 2025.

[5] A. Alabsi *et al.*, "Wireless Power Transfer Technologies, Applications, and Future Trends: A Review," *IEEE Transactions on Sustainable Computing*, pp. 1–18, 2024.

[6] W. Yang *et al.*, "Secure Charging Scheduling in Wireless Rechargeable Sensor Networks," *IEEE Transactions on Mobile Computing*, vol. 25, no. 2, pp. 1870–1884, 2026.

[7] O. M. Rosabal *et al.*, "Sustainable RF Wireless Energy Transfer for Massive IoT: Enablers and Challenges," *IEEE Access*, vol. 11, pp. 133 979–133 992, 2023.

[8] Z. Xue *et al.*, "Thermal Effect-Aware Wireless Rechargeable Sensor Networks," *IEEE Transactions on Networking*, vol. 34, pp. 442–456, 2026.

[9] Z. J. Chew *et al.*, "Power Management Circuit for Wireless Sensor Nodes Powered by Energy Harvesting: On the Synergy of Harvester and Load," *IEEE Transactions on Power Electronics*, vol. 34, no. 9, pp. 8671–8681, 2019.

[10] Z. Cai *et al.*, "Battery-Free Wireless Sensor Networks: A Comprehensive Survey," *IEEE Internet of Things Journal*, vol. 10, no. 6, pp. 5543–5570, 2023.

[11] Y. Liu *et al.*, "Rethinking Sustainable Sensing in Agricultural Internet of Things: From Power Supply Perspective," *IEEE Wireless Communications*, vol. 29, no. 4, pp. 102–109, 2022.

[12] P. Du *et al.*, "AI-Based UAVs 3-D Coverage Deployment in 6G-Enabled IoV Networks for Industry 5.0," *IEEE Transactions on Consumer Electronics*, vol. 71, no. 2, pp. 4221–4234, 2025.

[13] C. Lin *et al.*, "Near Optimal Charging Schedule for 3-D Wireless Rechargeable Sensor Networks," *IEEE Transactions on Mobile Computing*, vol. 22, no. 6, pp. 3525–3540, 2023.

[14] H. Dai *et al.*, "Placing Wireless Chargers With Multiple Antennas," *IEEE Transactions on Mobile Computing*, vol. 23, no. 6, pp. 7517–7536, 2024.

[15] C. Lin *et al.*, "Maximizing Charging Utility With Fresnel Diffraction Model," *IEEE Transactions on Mobile Computing*, pp. 1–15, 2024.

[16] W. Yang *et al.*, "Precise Wireless Charging in Complicated Environments," *IEEE/ACM Transactions on Networking*, pp. 1–16, 2024.

[17] W. Yang *et al.*, "Accurate 3D Wireless Charging," *IEEE Transactions on Mobile Computing*, vol. 24, no. 6, pp. 4733–4746, 2025.

[18] N. V. Bhalerao *et al.*, "3-D AAV Deployment for Maximizing Harvested Energy in WRSNs: A Soft Actor-Critic Approach," *IEEE Internet of Things Journal*, vol. 12, no. 9, pp. 12 083–12 093, 2025.

[19] Q. Guo *et al.*, "AoI-Constrained Efficient 3-D Far-Field Wireless Charging and Data Collection Using Multiple AAVs," *IEEE Internet of Things Journal*, vol. 12, no. 10, pp. 14 067–14 079, 2025.

[20] B. Clerckx *et al.*, "Fundamentals of Wireless Information and Power Transfer: From RF Energy Harvester Models to Signal and System Designs," *IEEE Journal on Selected Areas in Communications*, vol. 37, no. 1, pp. 4–33, 2019.

[21] C. Psomas *et al.*, "Wireless Information and Energy Transfer in the Era of 6G Communications," *Proceedings of the IEEE*, vol. 112, no. 7, pp. 764–804, 2024.

[22] M. A. Halimi *et al.*, "Rectifier Circuits for RF Energy Harvesting and Wireless Power Transfer Applications: A Comprehensive Review Based on Operating Conditions," *IEEE Microwave Magazine*, vol. 24, no. 1, pp. 46–61, 2023.

[23] N. Ayir *et al.*, "Practical Waveform-to-Energy Harvesting Model and Transmit Waveform Optimization for RF Wireless Power Transfer Systems," *IEEE Transactions on Microwave Theory and Techniques*, vol. 71, no. 12, pp. 5498–5514, 2023.

[24] D. Sarkar *et al.*, "Computational Intelligence for Modeling and Optimization of RFEH and WPT Systems: A Comprehensive Survey," *IEEE Microwave Magazine*, vol. 24, no. 9, pp. 46–60, 2023.

[25] V. Palazzi *et al.*, "Radiative Wireless Power Transfer: Where We Are and Where We Want to Go," *IEEE Microwave Magazine*, vol. 24, no. 2, pp. 57–79, 2023.

[26] M. Y. Naderi *et al.*, "Wireless sensor networks with RF energy harvesting: Energy models and analysis," in *2015 IEEE Wireless Communications and Networking Conference (WCNC)*, 2015, pp. 1494–1499.

[27] J. Xu *et al.*, "Robust Fault-Tolerant Placement of Wireless Chargers for Directional Charging," *IEEE Transactions on Mobile Computing*, vol. 23, no. 5, pp. 5295–5309, 2024.

[28] Z. El Khaled *et al.*, "Log Distance Path Loss Model: Application and Improvement for Sub 5 GHz Rural Fixed Wireless Networks," *IEEE Access*, vol. 10, pp. 52 020–52 029, 2022.

[29] C. Lin *et al.*, "Maximizing Charging Efficiency With Fresnel Zones," *IEEE Transactions on Mobile Computing*, vol. 23, no. 1, pp. 612–629, 2024.

[30] Z. Xu *et al.*, "Personalized Federated Learning-Based Distributed Model Predictive Control With Predictive Error Compensation for Nonlinear Networked Systems," *IEEE Transactions on Automation Science and Engineering*, vol. 22, pp. 20 837–20 853, 2025.